

Vibration Analysis at Microscale by Talbot Fringe Projection Method¹

R. Rodriguez-Vera*, K. Genovese[†], J. A. Rayas* and F. Mendoza-Santoyo*

*Centro de Investigaciones en Optica, Loma del Bosque 115, Col. Lomas del Campestre, León, Mexico

[†]Dipartimento di Ingegneria e Fisica dell'Ambiente (DIFA), Università degli Studi della Basilicata, Viale dell'Ateneo Lucano 10, 85100 Potenza, Italy

ABSTRACT: This work focuses on the implementation of a structured light projection technique for the analysis of the 3D vibration modes of microsamples. The Talbot image of a Ronchi grating is projected onto the sample surface passing through one of the objective tube of a stereomicroscope thus realising a fringe projection system at a micrometric scale. An aluminium cantilever beam PZT-driven into harmonic vibration served as test sample for investigating the possibility to get the full-field vibration modes of micro-objects. An automated Fourier transform analysis of the fringe patterns was performed to obtain the full-field time-resolved profile information of the sample at each frame delivered by a high-speed camera with a micrometric resolution. A straightforward procedure for retrieving resonance frequency for different modes and vibration amplitudes along the whole sample surface was implemented. The great sensitivity and the full-field capacities of the proposed experimental procedure allow to put in evidence differences between real and theoretical behaviours hence could be extremely useful for designing and testing structural dynamic response of microstructures and micro-electro-mechanical Systems.

KEY WORDS: *contouring, optical metrology, profilometry, Talbot fringe projection, vibration analysis*

Introduction

Nowadays, micro-electro-mechanical system (MEMS) is an emerging technology that introduces several challenges for their design and testing [1, 2]. From a structural dynamics point of view, characterisation of MEMS needs the identification of the resonant peaks in the vibration spectrum [3]. Experimental testing of vibration modes of microstructures, in fact, is demanded for determining the vibration response level in operation and for validating theoretical and numerical models. Moreover, experimental measurements are essential to evaluate some dissipative effects such as fluid/air damping that cannot be neglected when dealing with micro-featured structures.

Several optical techniques are already available for measuring out-of-plane vibration of microcomponents. Laser deflection [4] and laser Doppler

vibrometry [5, 6] are simple and reliable point measurement methods, while interferometry [7, 8], electronic speckle pattern interferometry [9, 10], photomicrography [11] provide a full-field map of the out-of-plane displacement of vibrating structures. As quality factors of the resonance describing different forms of energy losses can be reliably assessed only by considering the whole sample surface, full-field methods are surely to be preferred to point measurement when dealing with vibration of microdevices.

In this paper, we explore the possibility to apply a full-field non-contact optical method based on the Talbot effect [12] for the measurement of the vibration shapes of micro-objects. This method belongs to the fringe projection techniques that have already been extensively used in the microscopic range for 3D surface contouring with high lateral and vertical resolution [13–17]. In the proposed set-up, the Talbot image of a Ronchi grating is projected onto the sample surface passing through one of the objective tube of a stereomicroscope thus realising a fringe projection system at a micrometric scale. The deformed grating is acquired by a

¹Part of this paper was presented in 9th International Symposium on MEMS and Nanotechnology (9th – ISMAN), at the SEM XI International Congress & Exposition on Experimental & Applied Mechanics. June 2–5, 2008, Orlando, Florida, USA.

high-speed camera; the full-field phase map of the specimen surface can be straightforwardly obtained by performing a Fourier transform analysis [18]. System parameters such as grating period, illumination and observation angles, and calibration factor then serve to get whole-field topographic information from phase map hence realising the vibration 3D profiling of the microobject under investigation at the video acquisition rate.

Accuracy and resolution of the proposed Talbot fringe projection system was previously evaluated by contouring a calibrated sample [19]. Then, an aluminium cantilever beam undergoing in harmonic vibration through a piezoelectric translator (PZT) served as test sample for the dynamic measurement. Out-of plane shape of the resonant frequencies corresponding to the flexural vibration modes can be retrieved by performing a sinusoidal fitting of topography data for a series of control points chosen along the specimen surface. It has been demonstrated that, with the proposed methodology, frequency and amplitude of vibration can be obtained for all over the surface points with micrometric resolution.

The Fringe Talbot Projection Profilometer

When a linear grating of period p is illuminated by a collimated monochromatic beam, multiple identical images of the original grating are observed along the path of the light, as shown in Figure 1. These images are formed without any lenses on integer multiples of a distance called the Rayleigh distance (Δ). This phenomenon is known as the Talbot effect (self-imaging) and it is caused by the diffraction that suffers the light when pass through the grating [20]. The Talbot planes are located at distances given by:

$$\Delta_n = n \frac{p^2}{\lambda}, \tag{1}$$

where $n = 1, 2, 3, \dots$ (order of Talbot planes) and λ is the illumination light wavelength.

If a Talbot fringe image is projected on a surface target, as shown in Figure 2, fringes are deformed according to the surface profile [21]. If the object is a parallel plane to the grating, the fringe pattern will be identical to this one; but if the object has an irregular topography, the observed fringe pattern will present

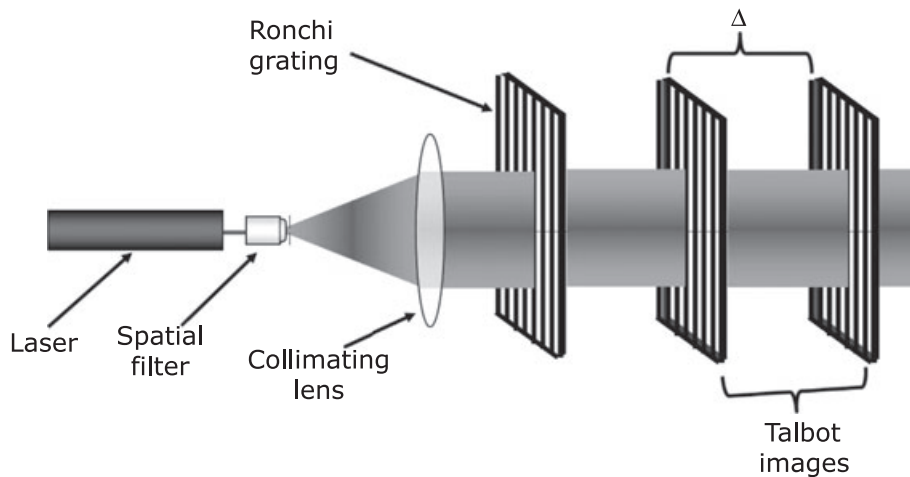


Figure 1: The Talbot effect produced when a grating is illuminated by a collimated wavefront

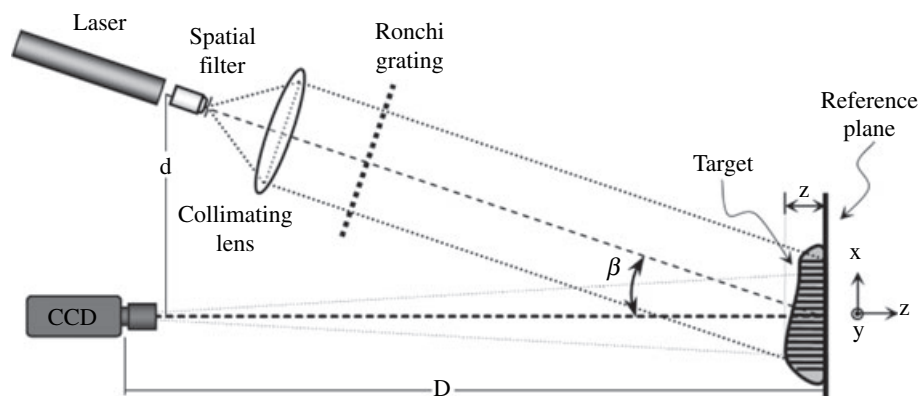


Figure 2: Setup of the Talbot-projected fringe profilometry

a deformed Talbot fringe image. This image is a codified optical signal and is captured by a charge-coupled device (CCD) camera for posterior digital processing. CCD get a fringe pattern phase modulated which is modelled by

$$I(x, y) = A + B \cos \frac{2\pi}{p_x} [x - z(x, y) \tan \beta], \quad (2)$$

where A and B are constants related to the target reflectivity with bias and modulation index, respectively. $p_x = p/\cos\beta$ is the observed period. This phase modulated fringe pattern should be digitally treated by several methods like that of the reference [18] to extract the optical phase map and afterwards the target profile from the unwrapped phase. The height, $z(x, y)$, to optical phase, $\phi(x, y)$, relationship for this case is given by [18]:

$$z(x, y) = \frac{D\phi(x, y)}{2\pi\nu_0 d + \phi(x, y)}, \quad (3)$$

where D is the distances between a reference plane and entrance pupils of the projection and viewing optical systems, d is the distance of separation of entrance pupils of the projection and viewing optical systems, and ν_0 is the observed grating frequency.

The Stereomicroscopic System

Figure 3A shows a scheme of the experimental stereomicroscope used to recover static and dynamic profiles of surface target. A 4 mW, 0.633 μm wavelength He-Ne laser is employed as illuminating source. The laser beam is expanded by a 40 \times micro-

scope objective and filtered by a 15- μm diameter pinhole. A 5 cm diameter and 15 cm focal length collimating lens is employed to illuminate a Ronchi grating. To facilitate the illumination and observation of the surface object, a ZEISS stereomicroscope (Carl Zeiss Microimaging GmbH, Jena, Germany), Stemi 2000-C model (Carl Zeiss Microimaging GmbH) (Figure 3B) is employed. Stereo angle can be tuned from 11 $^\circ$ to 16 $^\circ$ and magnification of the microscope's objective runs from 0.65 \times to 5 \times , because the microscope has a zoom assembly. Distance work to the maximum amplification is 3 cm and minimum vision area is 235 μm^2 .

One of the oculars (actually without it) is used for illumination and the other one for observation. Before capture the fringe pattern on the surface target, it is illuminated with white light to obtain the best focus. After, the target is illuminated by the Talbot fringe pattern moving the grating up to it is observed clear. In this case observed target by the microscope ocular imaging a reduced size Talbot plane. This means that this part of the microscope is used in inverse form. As a result, grating frequencies up to 100 lines per mm can be seen. Image of the fringe pattern produced by the observation ocular is captured by a 640 \times 480 pixels digital CCD camera. Images are digitised in 512 \times 480 and 8 bits.

Projected Fringe Pattern and the Fourier Method

When a Ronchi ruling is projected on a homogenous cantilever which is subjected to harmonic vibration (Figure 4), its behaviour can be considered as a time-

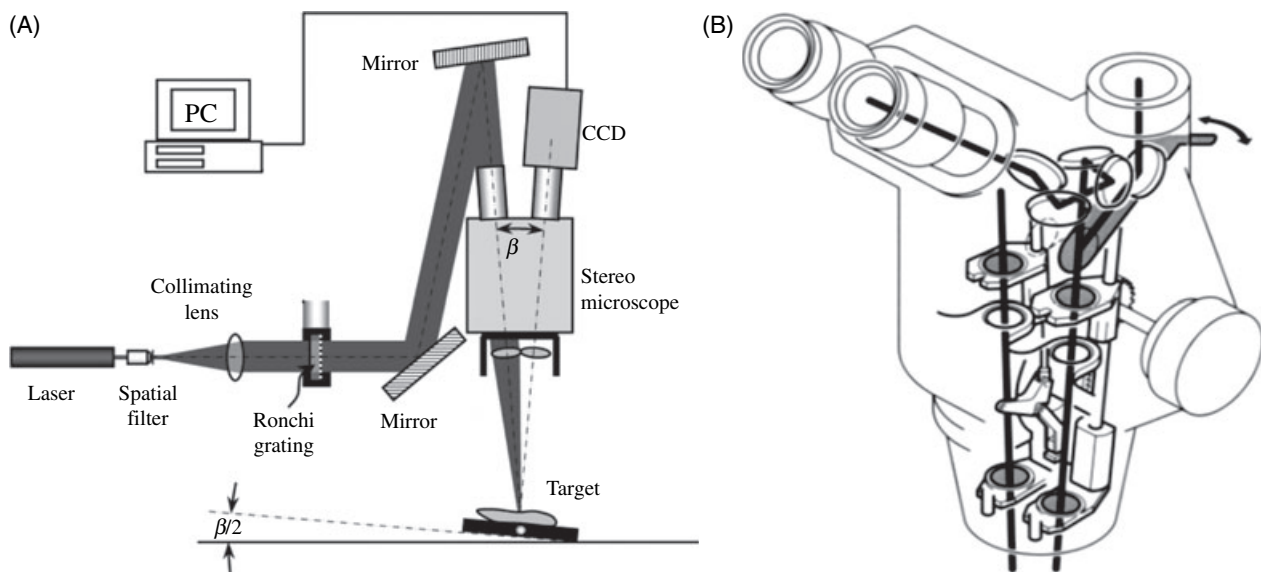


Figure 3: The stereomicroscope used for Talbot-projected imaging and vibration analysis. (A) Experimental scheme, b is the stereo angle. (B) Internal scheme, ZEISS stereomicroscope, Stemi 2000-C model

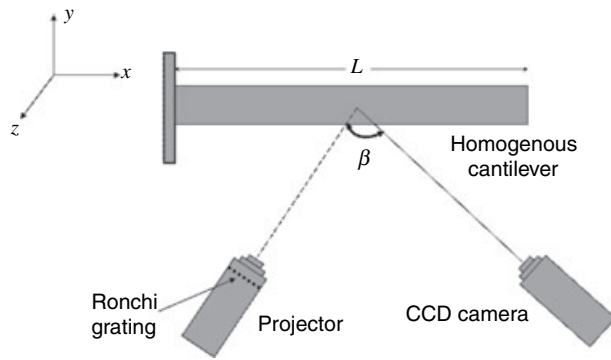


Figure 4: Experimental schematic setup, a Ronchi grating is projected on a homogenous fixed-end cantilever beam of length L and the image is captured by a CCD camera. Optical axes of the projector and CDD form an angle β . Projector optical axis is placed along the z -axis

varying interference pattern that contains a constant carrier frequency in the horizontal direction, given as [22]:

$$I(x, y, t) = a(x, y) + b(x, y) \cos[\phi(x, y, t) + 2\pi\mu_0 x], \quad (4)$$

where $a(x, y)$ and $b(x, y)$ are not time-dependent and are interpreted as the background and modulation intensities, respectively, $\phi(x, y, t)$ is the phase function at instant t , interpreted as the deformed grating on the cantilever surface. It should be pointed out that $\phi(x, y, t)$ also depends of the geometry of the experimental setup (Figure 4). The angle β , is that made between optical axes of projector and CCD camera. $\phi(x, y, t)$ depends on Ronchi ruling period $P = 1/\mu_0$, being μ_0 the carrier frequency. For a point (x, y) on the harmonically vibrating cantilever, the value of the phase is changing with time from maximum to minimum values as a result of the varying amplitude. Then, the phase measurements will give directly the cantilever contour from a vibration resonant mode.

To avoid time averaging, it is necessary to consider that the integration time of the CCD camera is smaller than the temporal period of the vibration cycle. Actually, this integration is 1/800 of a second [22]. Then, under this condition, any captured CCD frame of the fringe-projected pattern on the cantilever can be modelled as an interference pattern just as that expressed by Equation (4), that means,

$$I_k(x, y) = a(x, y) + b(x, y) \cos[\phi_k(x, y) + 2\pi\mu_0 x], \quad (5)$$

where the subscript k , is a positive integer that indicated the k -th captured pattern $I_k(x, y) = I(x, y, t_k)$ at time $t = t_k$. The term $2\pi\mu_0 x$ should not be larger than $a(x, y)$, $b(x, y)$ and $\phi_k(x, y)$ because the pattern of Equation (5) does not have a monotonous comporting, but it behaves according to the profile of the natural resonant mode of the cantilever.

To use the Fourier method [18], Equation (2) can be rewritten as

$$I_k(x, y) = a(x, y) + c_k(x, y) \exp(i2\pi\mu_0 x) + c_k^*(x, y) \exp(-i2\pi\mu_0 x), \quad (6)$$

where i is the unit imaginary number given by $\sqrt{-1}$, the symbol $*$ denotes the complex conjugated of $c_k(x, y)$, i.e.

$$c_k(x, y) = \frac{1}{2} b(x, y) \exp[i\phi_k(x, y)]. \quad (7)$$

The Fourier transform $\tilde{I}_k(\mu, y)$ of the recorded intensity distribution $I_k(x, y)$ is given by

$$\tilde{I}_k(\mu, y) = \tilde{A}(\mu, y) + \tilde{C}_k(\mu - \mu_0, y) + \tilde{C}_k^*(\mu + \mu_0, y). \quad (8)$$

As cited above, $a(x, y)$, $b(x, y)$ and $\phi_k(x, y)$ vary slowly compared with the carrier frequency μ_0 , hence the spectra are separated from each other by the carrier frequency μ_0 . One of the side lobes is weighted by the Hanning window and translated by μ_0 toward the origin to obtain $C_k(\mu, y)$. The central lobe and either of the two spectral side lobes are filtered out by translating one of the side lobes to zero frequency. Taking the inverse Fourier transform of $C_k(\mu, y)$ with respect to x yields $c(x, y)$. The phase distribution can then be calculated point wise using the expression

$$\phi_k(x, y) = \tan^{-1} \left\{ \frac{\text{Im}[c_k(x, y)]}{\text{Re}[c_k(x, y)]} \right\}, \quad (9)$$

where $\text{Im}[c_k(x, y)]$ and $\text{Re}[c_k(x, y)]$ denote the imaginary and real parts of $c_k(x, y)$, respectively. As the phase calculated results in values ranging from $-\pi$ to π , the phase distribution is wrapped in this range and consequently, phase unwrapping has to be carried out to remove any 2π phase discontinuities.

The local displacement of the object can be evaluated analyzing the phase value distribution of neighbouring points. For each k -th frame can be calculated the phase value distribution and obtain the contour or shape of the cantilever. In this case, phase value distribution was compared with a reference phase at time $t = 0$, that means by the cantilever in rest.

Calibration

The system shown in Figure 3 was mounted and then characterised in terms of such performance characteristics of longitudinal and transverse resolutions. We have also carried out calibration tasks for both

transversal and longitudinal directions for a fixed field of view of $2500 \mu\text{m}^2$.

Longitudinal and transverse resolution

The point spread function (PSF) is a measurement characterising the microscope imaging resolution. Theoretically, the transversal resolution is given by [23]:

$$r_{x,y} = \frac{0.61 \lambda}{NA}, \quad (10)$$

and the longitudinal by:

$$r_z = \frac{2 \lambda}{NA^2}, \quad (11)$$

where λ is the wavelength of light and NA is the numerical aperture of the objective lens, which is the sine of half of the observation angle of the lens multiplied by the index of refraction, n , of the material that is in between the lens and the sample. These limits, known as the diffraction limit, form the starting point for the struggle to improve the resolution; the narrower the PSF of a system, the better the resolution that can be achieved. Equations (10) and (11) are satisfied in the theoretical limit, that is, when the global optical system of the microscope is limited by diffraction. These same limits, in particular the traverse one, has to satisfy the Nyquist criterion to be able solve the projected fringes on the CCD array sensor matrix.

Transversal calibration

To determine the viewing area size observed for different magnification given by the microscope zoom assembly, a resolution certificated card was used. Images of the resolution card were digitised for three different magnifications as shown in Figure 5. In each case, was possible to determine the fringe pattern frequency and the total field of view.

From this, the *magnification factor*, $1.25\times$, is maintained for running all the tests. In fact, as the control of the objective magnification is continuous, to find the exact value of the magnification factor, a digitised image of the resolution card was processed by a simple MathCad[®] routine based on a threshold operation, in addition to the physical dimension of the digitised image pixel, which is $2.72 \mu\text{m}$. Under these considerations, the pitch of the observed projected fringe pattern was calculated to obtain $P = 15, 06$ pixels which correspond to $40.96 \mu\text{m}$. Based on these considerations, a *calibration factor* (CF) of $2.72 \mu\text{m}$ per pixel is taken. As the stereo angle of the microscope cannot be known with a great precision (it can be tuned from 11° to 16°), an inverse procedure was implemented to find the exact value of the angle involved for the measurement. This will be described below. Table 1 gathers all the parameters involved in the experiment for the traversal calibration.

Longitudinal calibration

As fringe projection is a geometric optical approach for 3D measurements of surfaces and components, the basic principle is the triangulation and it is well described elsewhere [15, 16, 24]. A structured light distribution is imaged onto the surface under a certain angle of incidence. The pattern is observed by a CCD camera from a different direction. In case of testing microstructures and microdevices, it is useful to take *telecentric* or at least nearly telecentric objectives for the illumination as well as for the detection. In this case, the relationship

$$z(x, y) = \frac{\phi(x, y) p_{\text{proj}}}{2\pi \tan \beta}, \quad (12)$$

is accepted. Being β the global angle between projection an observation direction respect to the surface target normal and p_{proj} is the projected grating pitch.

As is mentioned above, the stereo angle of the microscope cannot be known with a great precision.



Figure 5: (A) Resolution area 3338 mm^2 and frequency 5 lines per mm; (B) $1,540 \text{ mm}^2$ and 10 lines per mm; and (C) 235 mm^2 and 18 lines per mm

Table 1: Calibration parameters

Magnification factor	1.25
Pixel size	2.72 μm
Projected pitch	15.06 pixels
Projected pitch	40.96 μm
Calibration factor	2.72 μm per pixel
Projection optimised angle β^*	10.86°

*Optimisation process is described in Longitudinal calibration section.

An inverse procedure was implemented to find the exact value of the angle involved for the measurement. A perfectly flat plane was mounted on a micrometric translational stage and progressively moved in the z-direction of five 10- μm steps. The micrometric stage possesses a 1- μm resolution (10 μm division on the main micrometer plus a decimal nonio, hence $\pm 1 \mu\text{m}$ precision). The phase maps obtained were elaborated by the Fourier transform method [18] and the $z(x, y)$ map of the surface was obtained. While converting phase values in coordinates, an optimisation procedure was utilised to find the value of the projecting angle that minimise the error between calculated and target values. In particular, data points were first fitted with a plane and the relative distance between steps was calculated in function of the β angle. Then, iteratively, β was changed until the measured distance showed the minimum error with the expected 10 μm value. The optimisation problem has been formulated and solved with a *Sequential Quadratic Programming* (SQP) [25] routine, available in Matlab® (The MathWorks, Inc., Natick, MA, USA). SQP is a powerful optimisation technique, which employs quadratic approximations of cost function and linear approximations of constraints.

The problem is hence formulated as

$$\text{Min} \left[\Psi_{\text{plane}}(\beta) = \frac{1}{N} \sqrt{\sum_{j=1}^N (ax_j + by_j + cz_j + d)^2} \right] \quad (13)$$

where N is the number of control points, are the coefficients of the ideal plane equation and x_j, y_j, z_j are the optically measured coordinates of the j -th control point. The goal is to find β angle value that ensure the best fit between theoretical and measured geometry of the calibration target.

Optimisation brought to obtain an angle $\beta_{\text{opt}} = 10.86^\circ$ that has been used to plot experimental data (Figure 6). As it can be noticed by looking at the measured x - z profiles plotted in Figure 7, planes result slightly inclined. This is probably to ascribe to a not perfect alignment of the micrometric stage with the z-direction. However, the mean distance between

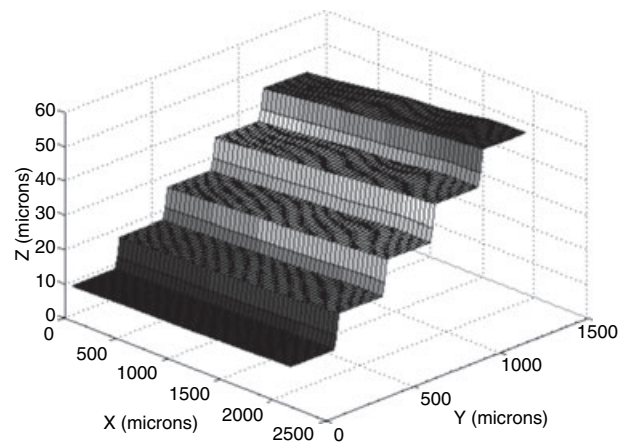


Figure 6: Stepwise planes obtained by moving a micrometric translational stage

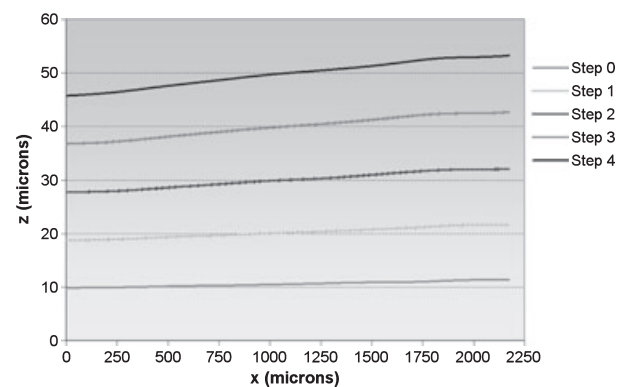


Figure 7: Profiles of the stepwise planes of Figure 6

parallel planes calculated over more than 3000 control points results to be 10 μm with a standard deviation of 0.6 μm . Figure 6 shows stepwise planes obtained by moving the micrometric translational stage which progressively is moved in the z-direction of five 10- μm steps. Profiles of the corresponding planes of Figure 6 are shown in Figure 7. As it is noticed, Figure 7 shows inclined planes, this is probably to human error. The plate was mechanically fixed by necked eye. However, this is a systematic error, which can be investigated to have a correction factor. And even this way, the inclination is quite small, of the order of 0.25°, which gives filling that at a big distance a bothersome amplification. Under these circumstances, it is possible to have accuracies of 1% laterally and 1–2% axially relative to the volume of the work space.

Vibration Analysis

To investigate the possibility to apply the proposed procedure for the dynamic profiling of vibrating structures at microscales, an aluminum

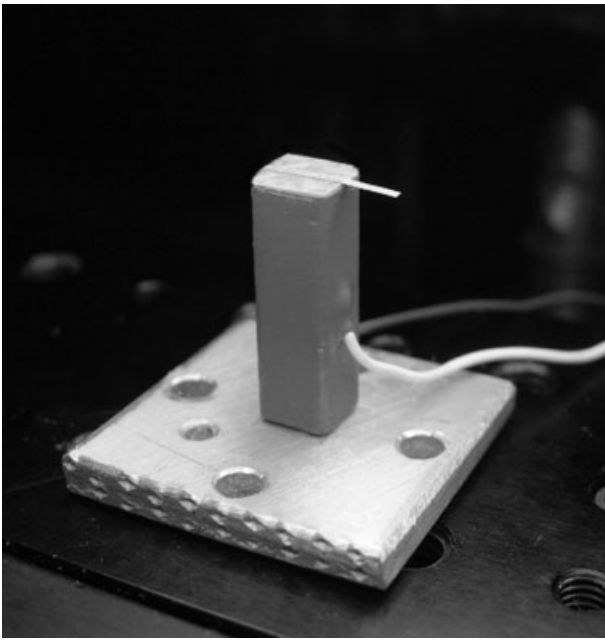


Figure 8: The aluminium micro-cantilever beam glued on the end of a PZT, used as sample for vibration analysis

beam (3960 μm long, 700 μm wide and 7 μm thick) cut from a very thin aluminium foil was glued on the top of a piezoelectric translator to realise the well theoretically known conditions of a vibrating clamped-free cantilever beam (Figure 8).

The best choice of optical and video-acquisition set-up parameters to get the desired sensitivity have been evaluated by performing a previous modal analysis with the commercial general purpose FEM code ANSYSTM to evaluate the expected natural frequencies and vibration amplitudes of the structure (Figure 9). The numerical model included 1276 nodes and 570 SOLID45 elements; aluminium material properties have been assigned to the model (Young's modulus $E = 70d + 9 \text{ N m}^{-2}$, Poisson's ratio $\nu = 0.35$, mass density $\rho = 2700 \text{ kg m}^{-2}$); kinematics

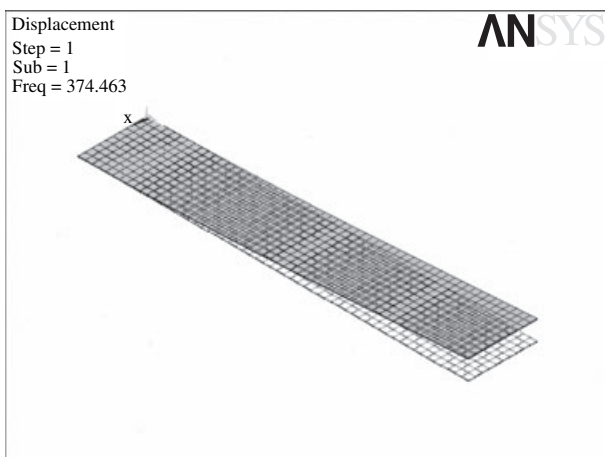


Figure 9: FEM simulated contour shape at the first resonance frequency

constraints reproduced experimental testing conditions. Modal analysis brought to find the first natural frequency at $f_n^{\text{num}} = 373.46 \text{ Hz}$. A very close result has been obtained by using the well-known equation for calculating the natural frequencies of a beam:

$$\omega_n = \alpha_n^2 \sqrt{\frac{EJ}{\rho A}}, \quad (14)$$

where, in the case of a cantilever beam, the boundary constants α_n are solutions of the equation:

$$\cosh(\alpha_n L) \cos(\alpha_n L) = -1, \quad (15)$$

where E is the Young's modulus, J the momentum of inertia, ρ the mass density, A the beam cross section and L its length. Equation (14) leads to find the first natural frequency at $f_n^{\text{th}} = 367.34 \text{ Hz}$. This preliminary analysis provided information to be used in defining testing parameters such as excitation amplitude and frequency range.

To perform a sufficient sampling of the first resonance vibration wave f_1 , a minimum frame acquisition rate (FAR) of $2f_1$ is required. The measurement data reported in this paper have been acquired at a FAR of 1135 fps. To obtain this camera FAR value, it was necessary to restrict the captured area to a central portion of the sample (5×1280 pixels) to get a satisfactory fringe visibility. However, pilot measurement carried out at lower FAR showed that captured data are sufficient to describe the flexural behaviour of the whole beam because deformation is fairly uniform along the beam width.

Based on fringe projection using the stereo-microscope described in The stereomicroscopic system section, an unmagnified Talbot self-image of a Ronchi ruling is imaged on the cantilever surface through one of the microscope oculars. The deformed fringe pattern is observed through the other microscope ocular on which the high-speed CCD camera is mounted to digitise the deformed fringe pattern. Digital fringe processing based on the Fourier method is carried out to have wrapped and unwrapped phase images for mapping to the measured profile (Figure 10).

The whole sample surface was previously focused under white light and its dimension and integrity was carefully checked before testing. Then, illumination was switched to laser light and the Al micro-cantilever was excited through the PZT actuator by applying a sinusoidal voltage generated by an EZ Digital (model FG-8002; EZ Digital Inc., Torrance, CA, USA) waveform generator. The displacement induced by the PZT translation (5 μm peak to peak)

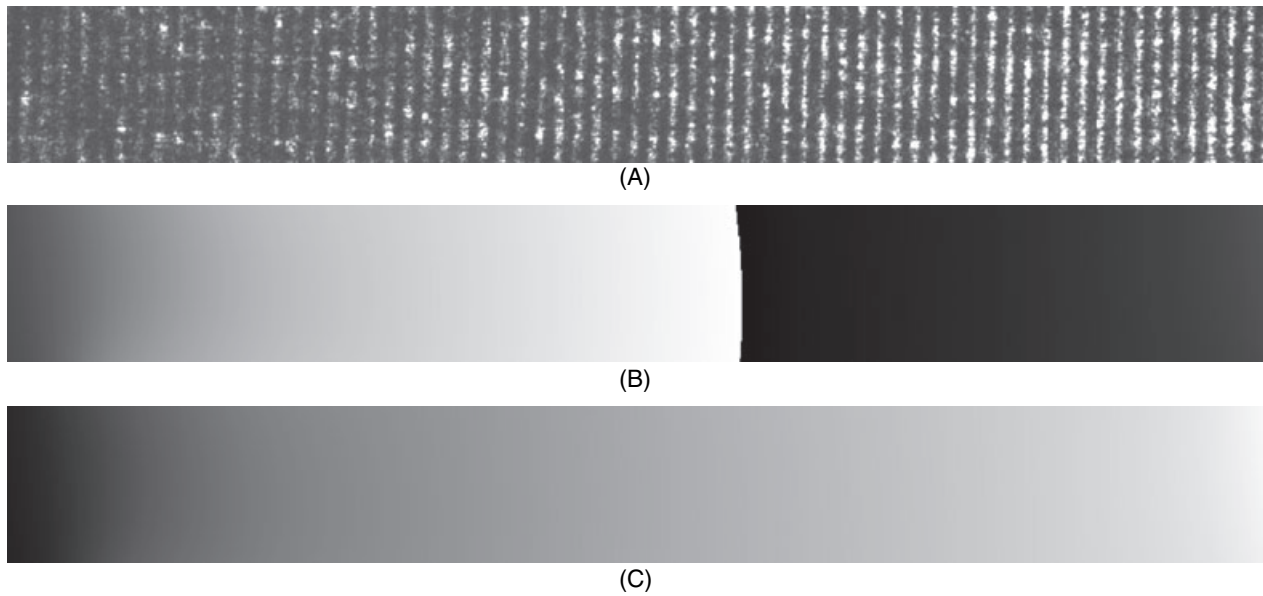


Figure 10: Optical experimental results for the first vibration mode of the micro-cantilever beam. (A) Projected fringe pattern; (B) wrapped phase map; and (C) unwrapped phase map

was set to lie below the sensitivity of the system. In this way, only when the first resonance frequency was encountered a large shift of the projected fringe pattern was easily distinguished close to the beam free end. As the chosen magnification factor allowed framing the whole specimen surface, no phase ambiguities because of 2π jumps arose being the deformation continuous from the fixed constrained edge. For each acquired image, the phase map was extracted (as the example in Figure 10) by performing a Fourier Transform analysis because it is a robust method that requires only one image [18]. In fact, even if phase-stepping methods could have the advantage to eliminate aberration errors, they require $N > 3$ images for each deformed state thus cannot be implemented when real-time measurements are entailed. In addition, the efficient filtering capabilities of the FT method allow removing laser speckle noise. A straightforward and fast unwrapping algorithm ‘by lines’ was sufficient to recover the $\phi_k(x, y)$ map because of the straight nature of the fringe pattern. The entire procedure for processing the fringe patterns was coded in the Labview™ (National Instruments, Austin, TX, USA) environment.

From phase values, the desired time-resolved beam profile was obtained (Figure 11) and amplitude versus time raw data related to five control points along the longitudinal beam section as indicated in Figure 11 were plotted into a graph. As expected, edge effects resulted in high errors close to the borders, thus displacement has been evaluated for a set of control points located at a proper distance d from the edges ($d = 800, 1300, 1800, 2300, 2800 \mu\text{m}$ from the constrained end; points G, J, K, L, M, respectively).

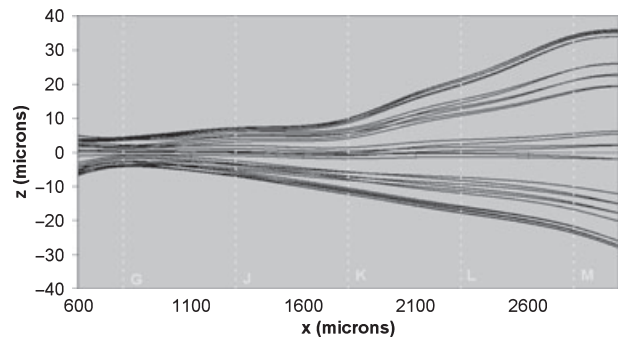


Figure 11: Time-resolved profiles of the vibrating micro-cantilever beam (continue lines, no smoothed) and control sections (dashed lines) for the analysis of vibration frequency and amplitude

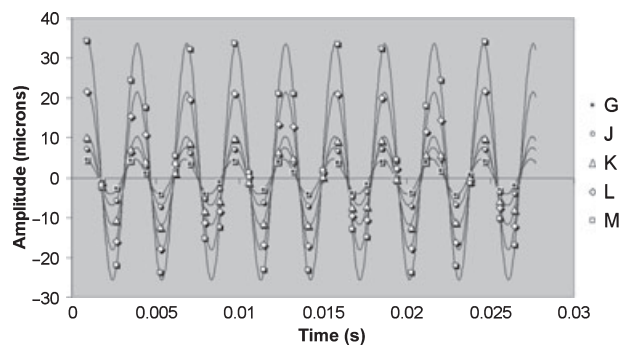


Figure 12: Measured oscillation of the microbeam at five control points fitted with sinusoidal waves (FAR = 1135 fps)

The optically measured data were fit to the equation of a sinusoid by a Least Square Error (LSE) approach coded in the Matlab™ environment (Figure 12). The fitting process served to find frequency, amplitude and mean value of the oscillation for each control point considered for the analysis. More pre-

Table 2: Summary of measurement data for the first resonance frequency

Control point	Amplitude (μm)	Mean value (μm)	Phase (radians)	Frequency (Hz)	Fitting error ψ (Hz)
G	4.3002	0.2586	-0.183	338.6025	0.0723
J	7.1755	0.3058	-0.336	338.4583	0.0469
K	11.0125	-0.7661	-0.427	338.8308	0.0848
L	19.7647	1.6832	-0.438	338.4573	0.0478
M	29.6598	3.9947	-0.44	338.2966	0.177

cisely, the parameters defining the sinusoidal wave (i.e. frequency f_1 , amplitude I_a , mean value I_m and initial phase ϕ) have been included as variables in the LSE problem aimed to minimise the difference between the j -th measured oscillation z_j^{ex} and the theoretical counterpart z_j^{th} at time t_j . A number of at least 20 cycles were considered for the fitting. Once the optically measured oscillation has been fitted to the theoretical wave, mean value and deviation of f_1 from the theory have been calculated for each measurement point. Fitting error ψ reported in Table 2 has been calculated as:

$$\psi = \frac{1}{N} \sqrt{\sum_{j=1}^N (z_j^{\text{ex}} - z_j^{\text{th}})^2}. \quad (16)$$

From the whole set of measurement, the evaluated first resonance frequency is $f_1 = 338.53$ Hz (standard deviation is as small as 0.2). Remarkably, frequencies of waves profiles obtained from different longitudinal section of the sample were perfectly overlapping. Hence, even a low sampling rate is demonstrated to be sufficient to catch the beam oscillation (frame rate was almost three times the unknown frequency f_1 thus only slightly greater than the minimum frequency imposed by the Nyquist criterion).

Even if geometrical details of the sample were carefully taken from optical microscope images and beam thickness was checked with great precision with a Mitutoyo digital micrometre (Mitutoyo, Maplewood, NJ, USA) (with a resolution of $\pm 1 \mu\text{m}$) along the specimen length, there is a slight discrepancy between numerical and theoretical results and the experimental counterpart. This likely arises from a series of factors such as: mismatch between geometrical and material parameters of the models and real properties of the sample, existence of residual stresses because of sample preparation, air and internal dissipation effects, not perfectly constrained edge, etc.

Because of limitation on the FAR of the camera used for the test reported in this paper, it was not possible to profile the second deformed flexural mode ($f_2 \cong 2000$ Hz). However, the proposed procedure

can be theoretically applied to capture any vibrating deformed shape if a careful choice of optical parameters is done on the basis of the sample dimension and the required measurement resolution.

Conclusions

In this paper, we presented the application of a micro-contouring fringe-projection technique based on the Talbot effect for the dynamic measurement of the deformed shape of vibrating samples. Once the system was set-up, a micro aluminium cantilever beam excited with a PZT actuator was contoured at the first resonance flexural frequency. Experimental data were elaborated to find frequency and amplitude of the oscillation along the beam with lateral and longitudinal resolutions in the micrometre range. The strength of this approach consists in the no contact and full-field features that are particularly needed when dealing with microstructures. The surface profiles within the whole illuminated area can be measured simultaneously and no scanning process is needed thus avoiding errors in estimating relative phase differences. This feature makes the technique suitable for studying air damping, residual stresses or manufacturing faults effect on the quality factors of vibration. Furthermore, if coupled with suited numerical or theoretical evaluations, the proposed procedure could be used to implement inverse characterisation of mechanical properties of thin films or membranes.

ACKNOWLEDGEMENTS

Authors manifest their deep gratefulness for the partial support received from National Council of Science and Technology (CONACyT) and the Council of Science and Technology of the Guanajuato State (CONCYTEG).

REFERENCES

1. Senturia, S. D. (2000) *Microsystem Design*. Kluwer Academic Publisher, Dordrecht.
2. Osten, W. (Ed.) (2007) *Optical Inspection of Microsystems*. CRC Taylor and Francis, Boca Raton.

3. Lobontiu, N. (2007) *Dynamics of Microelectromechanical Systems*. Springer, New York.
4. Petersen, K. E. and Guarnieri, C. R. (1979) Young's modulus measurements of thin films using micromechanics. *J. App. Phys.* **50**, 6761–6766.
5. Drain, L. E. (1980) *The Laser Doppler Technique*. Wiley, Chichester.
6. Lawrence, E. M., Speller, K. E. and Yu, D. L. (2003) MEMS characterization using Laser Doppler Vibrometry. *Proc. Soc. Photo. Opt. Instrum. Eng.* **4980**, 51–62.
7. Petitgrand, S., Yahiaoui, R., Danaie, K., Bosseboeuf, A. and Gilles, J. P. (2001) 3D measurement of micromechanical devices vibration mode shapes by stroboscopic microscopic interferometry. *Opt. Lasers Eng.* **36**, 77–101.
8. Bosseboeuf, A., Gilles, J. P., Danaie, K., Yahiaoui, R., Dupeux, M., Puissant, J. P., Chabrier, A., Fort, F. and Coste, P. (1999) A versatile microscopic profilometer-vibrometer for static and dynamic characterization of micromechanical devices. *Proc. Soc. Photo. Opt. Instrum. Eng.* **3825**, 123–133.
9. Brown, G. C. and Pryputniewicz, R. J. (1988) Holographic microscope for measuring displacements of vibrating microbeams using time-averaged, electro-optic holography. *Opt. Eng.* **37**, 1398–4051.
10. Aswendt, P., Hofling, R. and Hiller, K. (1999) Testing microcomponent by speckle interferometry. *Proc. Soc. Photo. Opt. Instrum. Eng.* **3825**, 165–173.
11. Rembe, C., Tibken, B. and Hofer, E. P. (2001) Analysis of the dynamics in microactuators using high-speed cine photomicrography. *IEEE J. Micr. Syst.* **10**, 137–145.
12. Rodriguez-Vera, R., Rayas, J. A., Martinez, A. and Mendoza Santoyo, F. (2006) Micrometric topography measurement by imaging a Talbot projected fringe pattern. *Proc. 7th Int. Symposium on MEMS and Nanotechnology (7th – ISMAN), Presented at the 2006 SEM Annual Conf. and Exposition on Experimental and Applied Mechanics*, St Louis, MO, USA, 130–139.
13. Kujawinska, M. and Pryputniewicz, R. J. (1996) Micromechanical measurements: a challenge for photomechanics. *Proc. Soc. Photo. Opt. Instrum. Eng.* **2782**, 15–24.
14. Salbut, L. and Kujawinska, M. (2001) The optical measurement station for complex testing of microelements. *Opt. Lasers Eng.* **36**, 225–240.
15. Leonhardt, K., Droste, U. and Tiziani, H. J. (1994) Micro-shape and rough-surface analysis by fringe projection. *Appl. Opt.* **33**, 7477–7488.
16. Windecker, R., Fleischer, M. and Tiziani, H. J. (1997) Three-dimensional topometry with stereo microscopes. *Opt. Eng.* **36**, 3372–3377.
17. Windecker, R., Fleischer, M., Körner, K. and Tiziani, H. J. (2001) Testing micro devices with fringe projection and white-light interferometry. *Opt. Lasers Eng.* **36**, 141–154.
18. Takeda, M. and Mutoh, K. (1983) Fourier-transform profilometry for the automatic measurement of 3-D object shape. *Appl. Opt.* **22**, 3977–3982.
19. Rodriguez-Vera, R., Genovese, K., Rayas, J. A. and Mendoza-Santoyo, F. (2007) Calibration of a micro-topographic measurement system based on Talbot fringe projection. *Proc. 2007 SEM Annual Conf. and Exposition on Experimental and Applied Mechanics*, paper 83, Springfield, MA, USA.
20. Paturski, K. (1993) *Handbook of the Moiré Fringe Technique*. Elsevier, Amsterdam.
21. Rodriguez-Vera, R., Kerr, D. and Mendoza-Santoyo, F. (1991) 3-D contouring of diffuse objects by Talbot-projected fringes. *J. Mod. Opt.* **38**, 1935–1945.
22. Meneses-Fabian, C., Rodriguez-Vera, R., Rayas, J. A., Mendoza-Santoyo, F. and Rodriguez-Zurita, G. (2007) Surface contour from a low-frequency vibrating object using phase differences and the Fourier-transform method. *Opt. Commun.* **272**, 310–313.
23. Garini, Y., Vermolen, B. J. and Young, I. T. (2005) From micro to nano: recent advances in high-resolution microscopy. *Curr. Opin. Biotechnol.* **16**, 3–12.
24. Wang, Z., Du, H. and Bi, H. (2006) Out-of-plane shape determination in generalized fringe projection profilometry. *Opt. Express* **14**, 12122–12133.
25. Nocedal, J. and Wright, S. J. (2006) *Numerical Optimization*, 2nd edn. Springer Verlag, New York.